CRYSTAL GROWTH & DESIGN

pubs.acs.org/crystal

Article

Polymorph Selection of Zeolitic Imidazolate Frameworks via Kinetic and Thermodynamic Control

Edina Balog, Gábor Varga, Ákos Kukovecz, Ágota Tóth, Dezső Horváth, István Lagzi, and Gábor Schuszter*

Cite This: *Cryst. Growth Des.* 2022, 22, 4268−4276

Read Online

ACCESS | Metrics & More | Article Recommendations | Supporting Information

ABSTRACT: Exploring the kinetics of metal−organic framework crystallization is crucial in order to design novel synthesis methods benefiting from far-from-equilibrium conditions, such as flow, microfluidic, or gel-phase reactors. Herein we focus on zeolitic imidazolate frameworks (ZIFs) obtained in the reaction of 2-methylimidazolate and zinc ions as a model system. The room-temperature synthesis carried out in pure water solvent without the addition of any alkaline chemical yields a highly crystalline product with good conversion within minutes. The short-term kinetic characteristics were determined by a high-speed camera, the result of which was complemented by a UV−vis photometer based long-term investigation. At low concentrations and moderate linker excess, which facilitate sluggish coordination and precipitation, a fast colloid formation is followed by a delayed and remarkable recrystallization, which leads to the formation of a dense *dia*(Zn) polymorph of ZIF. Although this is the thermodynamically favored route, it should be avoided due to the nonporous structure of the product. The same stoichiometric excess of the linker ions together with higher concentrations gives rise to the production of the thermodynamically less stable polymorph of ZIF: i.e., ZIF-8 with a sodalite-like structure is obtained via kinetic control. Similar conclusions are drawn in the case of cobalt(II)-containing imidazolate frameworks, which highlights that kinetic control based polymorph selection might be achieved for other MOFs as well. Our kinetic results were supported by scanning electron microscopy, powder X-ray diffraction, nitrogen gas adsorption, and Fourier-transformed infrared and Raman spectroscopy.

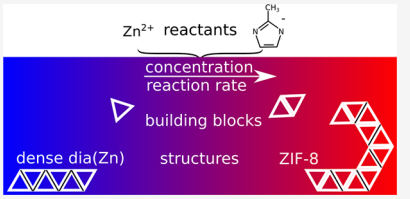

INTRODUCTION

Metal−organic frameworks (MOFs) are some of the most fascinating hybrid materials and are typically made of transition-metal cations (e.g., Zn^{2+} and Cu^{2+}) and various organic linkers (e.g., oxalic acid and terephthalic acid) and possess one-, two- or three-dimensional structures. MOFs have extremely high surface areas and pore volumes due to the special coordination nature of their building blocks.[1−5] Therefore, these materials have been proposed for diversified applications exploiting their unique behaviors in the high-pressure gas storage of hydrogen,[6,7] methane,[8,9] and carbon dioxide,[10] gas purification and separation,[11,12] heterogeneous catalysis,[13,14] photocatalysis,[15] targeted drug delivery,[16,17] electronics,[18,19] and sensors.[20,21] Recent studies have also proved their successful application in water harvesting from air even under desertlike arid conditions.[22] The versatile use of MOFs and the possibility of their prescribed and tailored synthesis has given rise to a new branch of chemistry called reticular chemistry.[23]

Traditionally, MOFs are synthesized through hydrothermal or solvothermal methods in the bulk phase, in which the reactants are mixed.[24−26] Recently, a new synthesis method has been proposed for producing zeolitic imidazolate frameworks (ZIFs) using a solid hydrogel medium with the combination of a coordination reaction and diffusion of metal cations and linkers.[27,28] In this setup, ZIFs with excellent crystallinity were spatially sorted in the gel column with continuously increasing crystal size ranging between 100 nm and 10 μm, which illustrates the great potential of the application of far-from-equilibrium synthesis methods.[27,28] However, the main drawback is the postsynthetic purification and separation of ZIFs from the gel components, which is a strong limitation for this approach in large-scale production. Therefore, the development of MOF synthesis methods utilizing concentration flux approaches in pure solvents and avoiding any postsynthetic size-selective purification is desired and challenging at the same time.[29] Similarly to other crystal growth systems, the formation of MOFs is governed by nucleation and crystal growth processes. In this context, the kinetic investigation of MOF formation is a crucial point in designing MOFs with an appropriate size and morphology, especially when crystallization is coupled to various transport phenomena, as in the discussed reaction−diffusion case or in microfluidic reactors. The nucleation kinetics of ZIFs was investigated by applying stopped-flow measurements coupled with time-resolved *in situ*

Received: March 1, 2022
Revised: May 6, 2022
Published: May 26, 2022

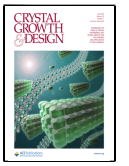

Downloaded via UNIV OF QUEENSLAND on November 14, 2022 at 22:21:15 (UTC).
See https://pubs.acs.org/sharingguidelines for options on how to legitimately share published articles.

ACS Publications

© 2022 The Authors. Published by American Chemical Society

https://doi.org/10.1021/acs.cgd.2c00265
Cryst. Growth Des. 2022, 22, 4268−4276

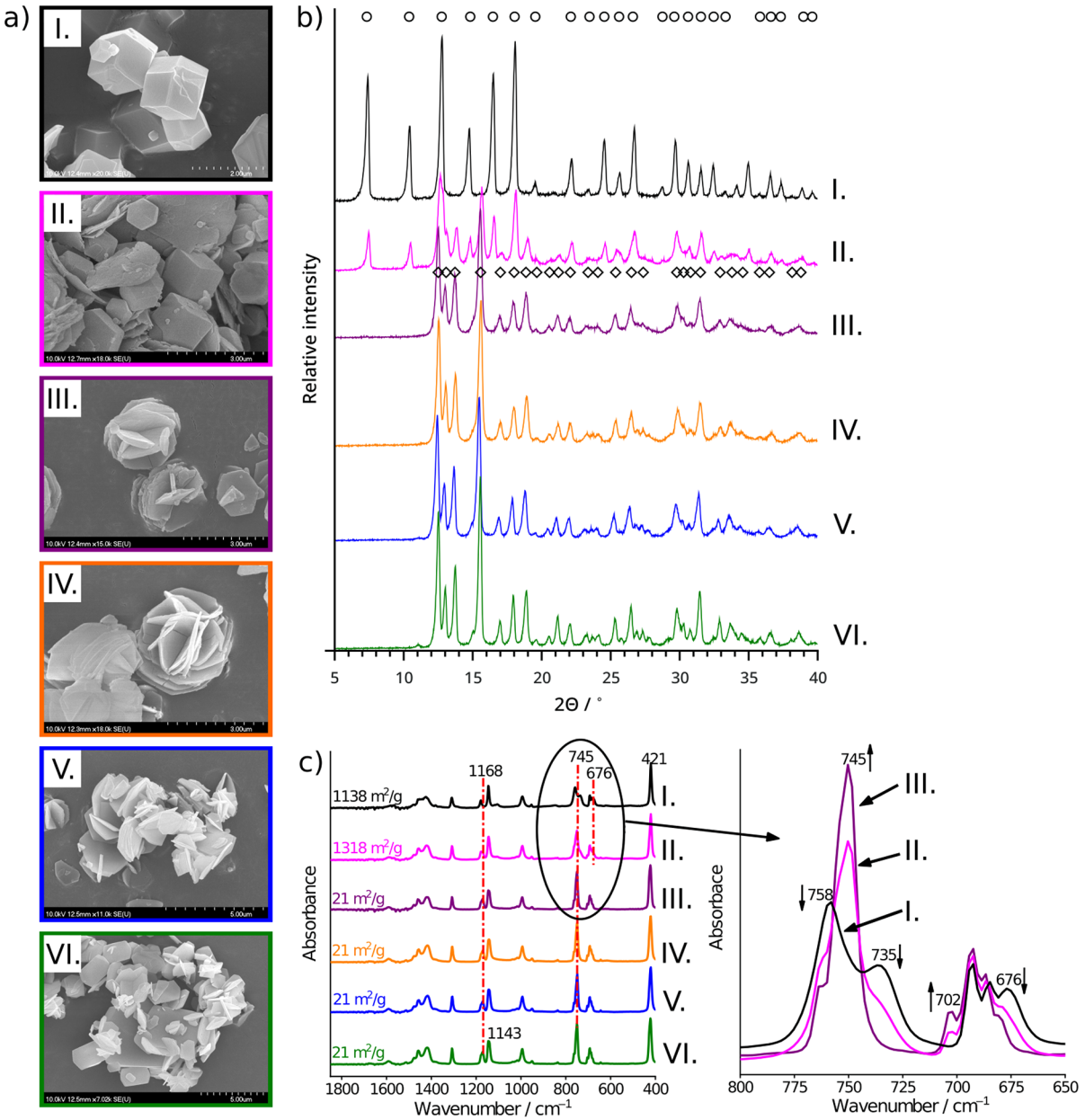

Figure 1. SEM micrographs (a), powder X-ray diffractograms (b), and Fourier-transformed infrared spectra (c) confirming the morphology, crystalline phase, and molecular structure transition, respectively, of the precipitate obtained at different solution compositions with fixed concentration ratios of (I) 500 and 25 mM, (II) 375 and 18.75 mM, (III) 250 and 12.5 mM, (IV) 160 and 8 mM, (V) 80 and 4 mM, and (VI) 30 and 1.5 mM of $[2\text{-MeIm}]_{tot}$ and $[Zn]_{tot}$, respectively. Identical roman numbers applied across the panels indicate identical initial solution compositions. Black circles and diamonds above the diffractograms correspond to reported diffractions of SOD and dense *dia*(Zn) polymorphs of ZIF, respectively.[41,43,47] The reaction time is 3 h in all cases.

small-angle and wide-angle X-ray scattering and liquid cell transmission electron microscopy.[30,31] Furthermore, the formation of core−shell and other complex precipitate particle structures was achieved in cobalt(II)- and zinc(II)-containing ZIFs by adjusting the reaction rates.[32] However, those syntheses were performed in methanol and did not focus on an investigation of the concentration-dependent precipitation. Herein, we investigate the kinetics of zeolitic imidazolate framework (ZIF) formation in the aqueous phase,[33−35] considering it to be a model reaction for MOF crystallization. The aqueous environment provides less optimal conditions for the synthesis in comparison with the use of less polar organic solvents, e.g., methanol and dimethylformamide, especially at room temperature. Minimizing the application of organic solvents contributes to maintaining a sustainable environmental development. Therefore, there is an increasing demand to develop green synthesis methods for the production of high-stability and -porosity MOF crystals in the aqueous phase.

ZIFs composed of zinc and 2-methylimidazolate ions possess three crystalline polymorphs that are interchangeable with more or less difficulties. While the SOD (sodalite-like) polymorph (ZIF-8) has a porous zeolite-like structure with high surface area, *kat* (katsenite-like) and *dia* (diamond-like) polymorphs have nonporous structures with a relatively low surface area.[36,37] Previous studies reported that the SOD polymorph exhibits significant sensitivity to an aqueous

https://doi.org/10.1021/acs.cgd.2c00265
Cryst. Growth Des. 2022, 22, 4268−4276

medium under ambient conditions at neutral *p*H.[38] The published results are divided on whether the formation of the dense *dia*(Zn) polymorph is a fundamental step before the total hydrolysis of the SOD polymorph into $Zn(OH)_2$ and imidazolate ions on immersion in water. It is also commonly accepted that the solidification of the dense *dia* polymorph is the thermodynamically favored process, which thus unfortunately enables the phase transformation of the SOD polymorph during syntheses.[36]

Although the thermodynamic stability difference between SOD and dense *dia*(Zn) phases is known in the literature,[36] the kinetic aspects of their competing crystallization has not yet been investigated. Therefore, we performed precipitation reactions in a well-stirred batch system and followed the morphology and chemical structure of the product over time in order to investigate whether a polymorph selection can be achieved via kinetic control.

RESULTS AND DISCUSSION

Synthesis in a Well-Stirred Batch System. MOFs belong to the subclass of coordination polymers: i.e., metal ions are coupled to each other via organic linkers. In the specific case of ZIF-8, Zn(II) ions are tetrahedrally coordinated by 2-methylimidazolate ions. In general, an excess of linker molecules increases the product quality: i.e., crystallinity. A significant amount of 2-methylimidazole (2-MeImH) is present in an aqueous solution in the form of deprotonated 2-methylimidazolate ion (2-MeIm^-) if the pH is around 14 ($pK_a \approx 13.8$;[39] a calculated speciation diagram is shown in the Supporting Information). Therefore, according to the literature, it is necessary to add a base to the reaction mixture to facilitate ZIF-8 formation in water.[40] It has also been shown that a properly selected base (e.g., NH_3) can contribute to the coordination reaction mechanism as well.[41] However, since 2-methylimidazole itself is a Brønsted base in water ($pK_a = 7.8$ for the conjugated acid[42]), moderately concentrated solutions may provide the appropriate alkaline conditions without adding any further alkaline ingredient.

In this context, we performed precipitation reactions in a well-stirred batch system to investigate the effect of reactant concentration on the crystalline phase and morphology of the forming crystals. Upon mixing of the aqueous solutions, the concentration ratio of the two reactants and thus the excess of 2-methylimidazole was kept constant ($[2\text{-MeIm}]_{tot}:[Zn]_{tot}$, = 20:1, where $[]_{tot}$ stands for the analytical concentration) to provide an ample amount of linker molecules. See the Supporting Information for further experimental details (solution preparation, crystalline phase assignment, microstructure analysis, Fourier-transformed infrared and Raman spectroscopic analysis, and nitrogen adsorption).

At $[2\text{-MeIm}]_{tot}$ = 500 mM concentration, the SOD polymorph (ZIF-8) is exclusively found after a 3 h reaction time according to the PXRD pattern and the SEM micrograph shown in Figure 1a-I,b-I. We highlight again that no additional alkaline ingredient was used; the aqueous mixture contained only zinc sulfate and 2-methylimidazole. To estimate the yield of the reaction, 50 mL portions of $[2\text{-MeIm}]_{tot}$ = 1000 mM and $[Zn]_{tot}$ = 50 mM solutions were mixed. After a 3 h reaction, the product was filtered and dried under ambient conditions. The mass of the obtained solid sample was 0.634 g, which corresponds to an ~56% yield because of the 2-MeIm:Zn^{2+} = 2:1 stoichiometry for the product. A slight decrease in the reactant concentrations ($[2\text{-MeIm}]_{tot}$ = 375 mM and $[Zn]_{tot}$ = 18.75 mM; SEM micrograph and PXRD pattern in Figure 1a-II,b-II, respectively) results in the appearance of a second crystalline phase in addition to the SOD polymorph, which is identified as a dense *dia*(Zn) structure according to the literature.[43] In this polymorph, some Zn(II) ions are coordinated to each other by two linkers; thus, a tetrahedral coordination is not fulfilled, which causes a smaller pore size and weaker adsorption capacity.[43] In the pictures, dense *dia*(Zn) has a lamellar structure in which the lamellae self-assemble into a 3D flowerlike structure. The SOD phase disappears upon further decreasing the reactant concentrations, and only dense *dia*(Zn) remains (SEM micrographs and PXRD patterns from III to VI in Figure 1a,b). Also, the flowerlike shape is less abundant at lower concentrations and is replaced by simple sheets, although the PXRD patterns are unchanged.

To further investigate the products, Fourier-transformed infrared (IR) and Raman spectroscopic studies were carried out on the solid samples obtained in the reactions performed with different initial concentrations. At the highest concentrations ($[2\text{-MeIm}]_{tot}$ = 500 mM and $[Zn]_{tot}$ = 25 mM), well-resolved characteristic vibration bands appear in the corresponding IR spectrum (Figure 1c-I), which are clearly associated with the vibration modes of ZIF-8. The relative intensities and the band positions of the vibrations are in good agreement with the reported vibrations of the SOD polymorph (Table S2).[44−46] We note here that, according to the PXRD, SEM, and IR results, the hydrolysis of the SOD polymorph did not occur under ambient conditions during the 3 h spent in aqueous solution. To distinguish between SOD and dense *dia*(Zn) polymorphs, vibration bands at around 1170 and 745 cm^{-1} corresponding to different ring vibrations of the heteroaromatic imidazolate ring are found to be useful markers (see Table S2 for band assignments). By a systematic decrease in the reactant concentrations, significant alterations in the marker regions are determined, which confirm a phase transition (enlarged region of Figure 1c). No vibrations of byproducts, including well-known hydrolysis products or reactants, are found. At $[2\text{-MeIm}]_{tot}$ = 250 mM and $[Zn]_{tot}$ = 12.5 mM and below, as a result of a complete phase transformation, vibration bands of the dense *dia*(Zn) polymorph are exclusively detected (curves from III to VI in Figure 1c). At intermediate concentrations ($[2\text{-MeIm}]_{tot}$ = 375 mM and $[Zn]_{tot}$ = 18.75 mM; Figure 1c-II), a combination of the typical vibration bands of the two polymorphs are registered, which indicates their coexistence. Accordingly, by fine-tuning the initial concentrations, both phase-pure polymorphs and their composites could be solidified under ambient conditions in aqueous solutions. This trend of the IR spectra is in line with the results of PXRD and SEM analysis.

Although less visible changes are seen, Raman spectra of the solid products also support the trend above (Figure S4 and Table S3). In addition, a notable change in the specific surface area of the samples is revealed via nitrogen adsorption measurements evaluated with the Brunauer−Emmett−Teller method (BET). The specific surface area differences are closely related to the polymorph structure. Pure dense *dia*(Zn) phase exhibits the lowest specific surface area (21 m^2/g), while a higher value is found for the SOD polymorph (1138 m^2/g), in good agreement with the literature.[48] The surface area of the novel polymorph mixture is close to that of ZIF-8 (1318 m^2/g).

https://doi.org/10.1021/acs.cgd.2c00265
Cryst. Growth Des. 2022, 22, 4268−4276

One may think that the crystalline phase change upon a decrease in the reactant concentrations is due to the pH of the solutions with different $[2\text{-MeIm}]_{tot}$. However, pH 10.8 is measured for 1000 and 750 mM 2-MeImH solutions as well (Table S1). In addition, pH 9.2 and 9.1 are obtained for the reaction mixtures with $[2\text{-MeIm}]_{tot}$ = 500 mM and $[Zn]_{tot}$ = 25 mM and $[2\text{-MeIm}]_{tot}$ = 375 mM and $[Zn]_{tot}$ = 18.75 mM, respectively. Since 2-methylimidazolate ion (i.e., the linker) is present in the solution in a small amount in this pH range (~0.1% of $[2\text{-MeIm}]_{tot}$; Figure S1a and Table S1), the solution speciation is quasi unchanged and thus not expected to largely affect the product, which contradicts the obvious trend seen in Figure 1. Furthermore, even in the case of the lowest reactant concentrations ($[2\text{-MeIm}]_{tot}$ = 30 mM and $[Zn]_{tot}$ = 1.5 mM), pH 9.9 is measured for the 2-MeImH solution and pH 8.9 for the reaction mixture, which cannot account for the prominent change in the crystalline phase and morphology.

As presented above, phase-pure ZIF-8 can be produced with good conversion in aqueous solution without the addition of any alkaline chemical next to the reactants. However, a phase change of the product from ZIF-8 to dense *dia*(Zn) is observed if the concentrations are appropriately lowered, but this is unlikely to be caused by the pH change of the reaction mixture. It is therefore assumed that the kinetics of the reaction determines the final product: i.e., there might be two different outcomes depending on the conditions. If the coordination and precipitation reactions advance rapidly, the thermodynamically somewhat unstable but kinetically stable product ZIF-8 may crystallize. On the other hand, sluggish coordination reaction and crystal growth forecasted by the lower reactant concentration may prefer the formation of the thermodynamically stable product (*dia*(Zn)). As our results prove, these kinetic aspects must be taken into consideration during the planning phase of experimental design, because they may ultimately influence the outcome of the synthesis.

Long-Term Kinetic Characteristics. Benchmark kinetic experiments showed that, shortly after the physical contact of the two aqueous reactant solutions ($ZnSO_4$ and 2-MeImH), the mixture becomes opaque, which indicates the formation of a colloid system. In contrast to this fast nucleation, crystal growth resulting in the appearance of a microscopic precipitate takes place on a longer time scale. The long-term kinetic investigation of a precipitation reaction can be carried out with the aid of a UV−vis spectrophotometer.[32,49] The turbidity of the dispersion changes with the concentration, shape, and size of the solid particles. We applied such a method for the kinetic study of ZIF formation. In one part of the experiments the compositions of the reaction mixtures were identical with those applied for the well-stirred synthesis presented above, while the effect of an increasing linker concentration at a fixed metal ion content was tested in separate measurements.

The reactant solutions were filled into a well-stirred and sealed photometric cuvette with different concentration ratios and various initial values. During the experiments, the turbidity (T) was measured over time (t) at 340 nm with a photometer (UV−vis PC spectrophotometer, VWR). Further experimental details may be found in the Supporting Information.

The graph in Figure 2a shows experimental results with a constant concentration ratio ($[2\text{-MeIm}]_{tot}$:$[Zn(II)]_{tot}$ = 20:1) and various solution compositions. We highlight that the color codes used for Figures 1 and 2 with respect to solution composition are identical to facilitate a direct comparison. It is observed in each case that T sharply increases immediately upon mixing the reactants. At the highest reactant concentration ($[2\text{-MeIm}]_{tot}$ = 500 mM and $[Zn(II)]_{tot}$ = 25 mM; Figure 2a-I), T maintains a high and constant value during the experiment. However, $T-t$ curves obtained with lower concentrations show a stepwise trend: i.e., a second turbidity increase is also detected. At somewhat lowered but still high

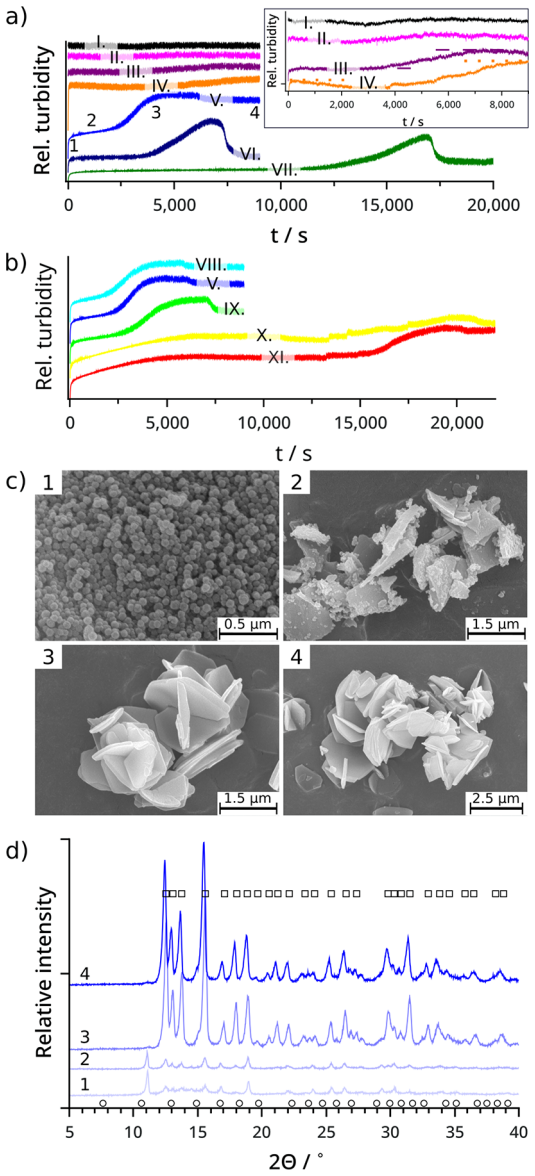

Figure 2. (a, b) Relative turbidity−time curves showing the crystalline phase transition taking place at different times as a function of solution composition. The curves are vertically shifted for better visualization. (a) Varying concentrations at constant ratio ($[2\text{-MeIm}]_{tot}$:$[Zn(II)]_{tot}$ = 20): (I) 500 and 25 mM, (II) 375 and 18.75 mM, (III) 250 and 12.5 mM, (IV) 160 and 8 mM, (V) 80 and 4 mM, (VI) 40 and 2 mM, and (VII) 30 and 1.5 mM of $[2\text{-MeIm}]_{tot}$ and $[Zn(II)]_{tot}$, respectively. The inset presents a closeup of the curves and the recrystallization steps. (b) Fixed $[Zn(II)]_{tot}$ = 4 mM and varying $[2\text{-MeIm}]_{tot}$: (VIII) 160 mM, (V) 80 mM, (IX) 40 mM, (X) 30 mM, and (XI) 20 mM. (c) SEM micrographs presenting the change of particle morphology along the V curve shown in (a) and (b); the numbering of the micrographs corresponds to the sampling instances shown in (a). (d) PXRD patterns corresponding to the SEM micrographs above, with serial numbers inscribed. Squares above and circles below the diffractograms belong to dense *dia*(Zn) and ZIF-8 diffractions, respectively.[41,43,47]

https://doi.org/10.1021/acs.cgd.2c00265
Cryst. Growth Des. 2022, 22, 4268−4276

concentrations (curves from II to IV in Figure 2a), the second step is shallow because the turbidity of the suspension is high and thus a further change is less dominant. Nevertheless, the inset in Figure 2a clearly shows that the height of the second step increases by lowering the concentrations. The same trend is even more pronounced at $[2\text{-MeIm}]_{tot}$ = 80 mM and $[Zn(II)]_{tot}$ = 4 mM concentrations (Figure 2a-V) and below. Not only the step height increases but also the onset time of the second step becomes longer in more dilute solutions (quantitative measures shown in Figure S5a).

To investigate the temporal change of the precipitate microstructure predicted by the stepwise $T-t$ curves, similar experiments with well-stirred mixtures were carried out in a larger volume (100 mL) with a $[2\text{-MeIm}]_{tot}$ = 80 mM and $[Zn(II)]_{tot}$ = 4 mM solution composition (Figure 2a-V,b-V). Samples were withdrawn from the beaker at selected characteristic times (assigned to curve V in Figure 2a): i.e., (1) at the very beginning of the reaction (450 s), (2) during the first plateau (1200 s), (3) at the end of the second step (4500 s), and finally (4) much later than the second step (10800 s). The samples were immediately filtered, washed with water, and dried under ambient conditions. The solid samples were analyzed as in the previous experiments (SEM, PXRD, and FTIR and Raman spectroscopy). Nanoparticles of 64 ± 6 nm size without a well-defined shape are found ∼7 min after maintaining supersaturation (Figure 2c-1). The measurement is based on 200 particles and an image analysis (ImageJ). The corresponding diffractogram of Figure 2d-1 shows that the degree of crystallinity is poor at this point of the reaction. During the period marked with nearly unchanged T, the initially formed nanoparticles rearrange into relatively thick sheets with particles on their surfaces (Figure 2c-2). The diffractogram shows that the amorphous character of the crystals decreases and that the characteristic peaks are more pronounced (Figure 2d-2). Approximately 90 min after the contact of the reactant solutions, 3D complex structures (Figure 2c-3) evolve from the sheets and this process is indicated by a prominent turbidity increase (Figure 2a-V3). The diffractogram indicates a high crystallinity (Figure 2d-3). The shape of the 3D crystals remains unchanged over the rest of the reaction; thus, this is the final product (Figure 2c-4). It also can be determined from the diffractograms that the crystalline phase changes during the reaction. The diffractogram of the final product is clearly assigned as dense *dia*(Zn) (Figure 2d-4 and black squares above the diffractograms). The reflections belonging to the nanoparticles present at the initial stage cannot be properly designated as ZIF-8 (Figure 2d-1 and black circles below the diffractograms). By monitoring of the effect of reaction time on the structure of the solids, FTIR and Raman spectra exhibit an interesting tendency. Both the positions and the relative intensities of the characteristic vibration bands associated with the dense *dia*(Zn) structure remain unchanged (Figure S6). Accordingly, in the quasi-amorphous structures identified by PXRD (Figure 2d-1,2), the first coordination spheres are the same, which are characteristic of the phase-pure dense *dia*(Zn) polymorph. This observation is a significant difference in comparison with previously published results, where these amorphous specimens generated during the syntheses or hydrolysis of ZIF-8 are assigned as the SOD structure.[38] Raman spectra of the products also remain unvariable over time, supporting the existence of the dense *dia*-like amorphous phase(s) (Figure S7).

A similar kinetic investigation was carried out with elevated concentrations ($[2\text{-MeIm}]_{tot}$ = 500 mM and $[Zn(II)]_{tot}$ = 25 mM). In good agreement with the Figure 2a-I curve, which shows no stepwise trend, the product is ZIF-8 over the entire reaction and no recrystallization is detected (diffractograms are given in Figure S8). The surface of the crystals collected at the very beginning of the reaction is somewhat rough. However, the samples collected at later stages depict a smooth surface and the typical ZIF-8 shape (SEM images of Figure S8).

The above findings prove that ZIF-8 is not the only accessible product of the reaction between Zn(II) ions and 2-MeImH. If the reactant concentrations are high and thus the coordination and precipitation reactions fast, ZIF-8 can be produced in aqueous solutions without the addition of any further alkaline chemical. However, lower concentrations and thus slower reactions lead to the formation of the dense *dia*(Zn) polymorph. This agrees well with the results obtained by density functional theory calculations: i.e., the latter species is the thermodynamically more stable phase[36] and ZIF-8 only can be yielded via kinetic control.

The graph in Figure 2b shows the results of kinetic experiments of well-stirred mixtures performed with increasing stoichiometric excesses of 2-MeImH while the zinc sulfate concentration is kept constant ($[Zn(II)]_{tot}$ = 4 mM). To facilitate the comparison of effects caused either by increasing the reactant concentrations at a fixed ratio or by varying the ratio at a fixed $[Zn(II)]_{tot}$, curve V simultaneously presented in Figure 2a,b serves as a reference ($[2\text{-MeIm}]_{tot}$ = 80 mM and $[Zn(II)]_{tot}$ = 4 mM). The second turbidity increase referring to recrystallization appears at ∼2200 s in Figure 2b-V. This onset time becomes slightly shorter (1900 s) upon increasing $[2\text{-MeIm}]_{tot}$ from 80 to 160 mM: i.e., increasing the stoichiometric excess from 20× to 40×. Also, decreasing $[2\text{-MeIm}]_{tot}$ from 80 to 40 mM, i.e., decreasing the stoichiometric excess from 20× to 10×, slightly elongates the onset time (∼2400 s). In contrast to these modest changes, further decreasing $[2\text{-MeIm}]_{tot}$ by a small amount (from 40 to 30 mM) is manifested as a jump in the length of the onset time: it suddenly becomes ∼12000 s (quantitative measurements are shown in Figure S5b). Therefore, even though the stoichiometric excess of the linker molecules is ensured at the lowest concentration as well ($[2\text{-MeIm}]_{tot}$ = 20 mM, i.e., 5× excess in comparison to $[Zn(II)]_{tot}$, and 2.5× more than that dictated by the stoichiometry of ZIF-8), the optimal onset time is reached at 10−20× excess. The two steps of the mechanism are more distinguishable at higher linker excesses. It is also observed that reaching approximately $[2\text{-MeIm}]_{tot}$:$[Zn(II)]_{tot}$ = 20:1 concentration ratio maximizes the yield, since a greater 2-MeImH excess did not provide either a larger amount of product or a significantly faster transition. A further important conclusion is that, since Figure 2b presents only stepwise $T-t$ curves independently of linker concentration, the synthesis of ZIF-8 cannot be carried out. Indeed, a higher $[Zn(II)]_{tot}$ is required to reach a sufficient initial reaction rate in order to avoid the formation of the thermodynamically stable product (dense *dia*(Zn)) and thus to maintain kinetic control on the process.

To investigate whether the phenomena observed for the Zn(II)−2-MeImH system (i.e. (1) distinct recrystallization steps at low concentrations and (2) polymorph selection by applying different reactant concentrations) are unique or applicable to other MOFs as well, we performed a similar set of experiments in the Co(II)−2-MeImH system. The production of zeolite-like ZIF-67 and dense *dia*(Co) structures under

https://doi.org/10.1021/acs.cgd.2c00265
Cryst. Growth Des. 2022, 22, 4268−4276

hydrothermal conditions on application of various cobalt salts is known in the literature.[50] Thus, these compounds might be obtained via our water-based room-temperature synthesis as well. In conjunction with the kinetic investigation of the Zn(II)−2-MeImH system, the turbidity of the reaction mixtures was followed with time for various solution compositions in the Co(II)−2-MeImH system as well. Similarly to the Zn(II)−2-MeImH system, stepwise $T-t$ curves are revealed (Figure S9a). Furthermore, the onset time of the second turbidity step again becomes shorter upon increasing the reactant concentrations (quantitative measurements are shown in Figure S5c). Finally, polymorph selection is also achieved by varying the reactant concentrations and maintaining a $[\text{2-MeIm}]_{tot}$:$[\text{Co(II)}]_{tot}$ = 20:1 ratio just as for the Zn(II)−2-MeImH system. According to the SEM and PXRD results, ZIF-67 crystals are produced even at the beginning of the reaction at high reactant concentrations, where the recrystallization step is barely present (Figure S9b). Application of lower concentrations, however, results in the production of dense *dia*(Co) particles (Figure S9c), in good agreement with the Zn(II)−2-MeImH system. These results highlight that the polymorph selection of various ZIFs might be feasible via kinetic control even in an aqueous medium at room temperature.

Short-Term Kinetic Characteristics. Although UV−vis experiments facilitate long-term kinetic characterization, they exclude investigation with high temporal resolution on a short term (<5 s), even though this is indeed the time scale of nucleation for ZIFs. The time scale of precipitation reactions is often characterized by the induction period, which is the time elapsed between maintaining supersaturation and detecting precipitation.[51−53] During the UV−vis experiments, T sharply increases immediately upon mixing the reactants; thus, the induction period cannot be determined by this method because of the ∼5 s dead time elapsing between solution mixing and data recording. To determine the short-term characteristic time scale of ZIF precipitation, the kinetics of colloid formation was captured with a high-speed-camera (HSC)-based method.[54]

In the HSC experiments, 350 μL of aqueous $ZnSO_4$ solution was injected from a height of 5 mm into a pool of 350 μL of an aqueous 2-methylimidazole solution contained in a standard spectrophotometric cuvet. The mixing of the two solutions generated by the impacting droplets together with the emerging cloudiness of the reaction mixture was recorded with a high-speed camera (Phantom Miro 110 equipped with a Nikon AF-S 105 mm f/2.8 IF ED VR micro objective). The detection was facilitated by transmitted light (cold white COB LED reflector, 8000 lm). The image sequence showing the dynamics of the system is presented in Figure 3a−c; further experimental details are given in the Supporting Information. The HSC method relies on tracking the gray-scale intensity of the photographs taken of the precipitation process, since the colloid dispersion scatters light. Therefore, the cumulative gray-scale intensity of the images in the sequence gradually decreases over time with a concentration-dependent trend, which allows us to determine the induction period (t_{ind}).[54]

Figure 3d depicts a typical gray-scale intensity−time data set for a HSC experiment. The gray-scale recording begins when the cuvet contains only the 2-MeImH solution. Then, at t = 0 s, the injection of the $ZnSO_4$ solution starts and I increases because the meniscus, which appears black in the image, leaves the field of view. Although Schlieren speckles evolve during

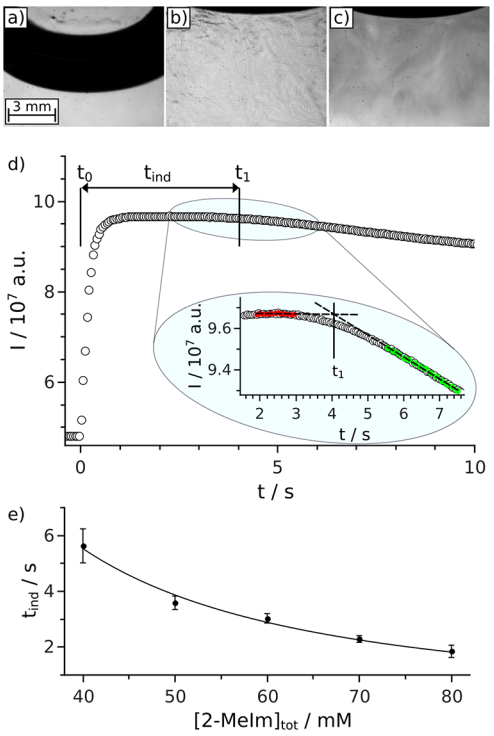

Figure 3. Snapshots of a typical HSC experiment: (a) side view of the meniscus of the 2-methylimidazole solution; (b) mixing of reactant solutions after the addition of $ZnSO_4$ solution; (c) emerging cloudiness caused by the formation of the colloid system below the liquid−air interface. The cuvet is positioned in such a way that its bottom and side edges are just outside of the field of view and the meniscus of the reaction mixture is close to the top of the image. (d) Induction period (t_{ind}) determination on the basis of the temporal evolution of the image gray-scale intensity (I). The inset shows an enlarged region of the entire data set for better visualization. Solution composition: $[\text{2-MeIm}]_{tot}$ = 50 mM and $[\text{Zn(II)}]_{tot}$ = 2.5 mM. (e) Concentration dependence of t_{ind} (constant ratio, $[\text{2-MeIm}]_{tot}$:$[\text{Zn(II)}]_{tot}$ = 20:1).

dropping because of the apparent refractive index difference of the solutions (Figure 3b), they do not interfere with the determination of t_{ind}. Later, the steep decrease of I is attributed to colloid formation, which scatters light and thus gives a cloudy appearance (Figure 3c). t_1 refers to the end of the induction period, which is determined as the intersection of the two lines fitted to the reference state (i.e., homogeneous solution) and to the colloid formation state (closeup in Figure 3d).

According to Figure 3e, t_{ind} strongly depends on the reactant concentrations even if their ratio is kept constant ($[\text{2-MeIm}]_{tot}$:$[\text{Zn(II)}]_{tot}$ = 20:1). Within the investigated concentration range, t_{ind} changes between 2 and 5.2 s. The concentration (c) dependence can be described by a power law ($t_{ind} = ac^{-b}$), where the exponent b is found to be 1.6 ± 0.1.

On the basis of our findings, the emergence of the colloid intermediate state can be considered quasi-instantaneous at concentrations relevant for large-scale ZIF-8 synthesis. This shall be taken into account when the product properties (particle size or crystallinity) are subjected to fine-tuning, since the growth rate of the crystals (and thus the final size of the particles) depends on the local mass fluxes of the components. Pronounced nucleation results in numerous nuclei; thus, the crystal growth might be hindered because of the depletion

https://doi.org/10.1021/acs.cgd.2c00265
Cryst. Growth Des. 2022, 22, 4268−4276

zones around them. As is proven by the UV−vis experiments, slow coordination and crystal growth may lead to the formation of the dense *dia*(Zn) phase instead of ZIF-8. Therefore, synthesis methods that can affect the nucleation step through coupled transport phenomena, e.g., microfluidic synthesis,[55,56] under the presence of flow and diffusive transport may benefit from such scaling laws.

CONCLUSION

By investigating the kinetics of ZIF formation with a high-speed camera and UV−vis spectrometer based techniques, we found that a colloid dispersion rapidly evolves after mixing the reactant solutions. The characteristic time of this colloid formation significantly shortens at higher concentrations. At appropriately low concentrations, slow recrystallization follows the colloid formation, which can be tracked by a remarkable turbidity increase via UV−vis measurements. Time-elapsed SEM micrographs and powder X-ray diffraction analyses prove that the morphology and crystallinity change during the reaction. At the same time, Fourier-transformed infrared and Raman spectroscopy results indicate that the product is dense *dia*(Zn) even at the beginning of the reaction.

It is shown that highly crystalline ZIF-8, as a thermodynamically less stable polymorph of ZIF, can be produced in aqueous solution at room temperature, without the addition of any alkaline chemicals next to the reactants, if the concentrations are high; thus, a kinetic control is maintained over the reaction. The synthesis is free of side products, and no sign of hydrolysis products is found.

A possible interpretation of the above kinetic control is the following. During the syntheses performed with a constant concentration ratio of the reactants, the solution speciation is quasi unchanged; only the reactant concentration varies. Therefore, one may speculate that zinc and imidazolate ions can transform into the product via two independent and competing routes that are characterized by different kinetic orders. For now, let us not consider whether ions or zinc−imidazole complexes participate in the reaction as building blocks in reality. Since dense *dia*(Zn) has a lamellar structure, independent building blocks may attach to each other one by one, which forecasts a small kinetic order. On the other hand, the 3D network of ZIF-8 may require the incorporation of larger (secondary) building blocks just as for zeolites (i.e., doublets of species in our case) with a characteristic spatial configuration. This latter step can involve only certain blocks and results in larger nuclei, thus exhibiting a larger kinetic order in comparison to dense *dia*(Zn) formation. Since the two routes are parallel but are characterized by different kinetic orders, that with a higher order is more sensitive to the change in reactant concentration. That is, the formation of ZIF-8 is hindered to a greater extent upon decreasing the concentration, unlike that of dense *dia*(Zn), as we observe throughout our experiments.

Furthermore, we presented that the above results are not exclusive for zinc(II)-containing imidazolate frameworks. Indeed, similar results were obtained utilizing cobalt(II) instead of zinc(II), which may forecast a feasible kinetic control for the synthesis of other MOFs as well.

As has been presented, maintaining high concentrations provides an appropriate kinetic control for ZIF-8 production, but it also results in fast nucleation and thus prescribes mass flux across the depletion zone around the particles during crystal growth. These antagonistic effects should be taken into account when synthesis methods relying on far-from-equilibrium conditions are elaborated: e.g., microfluidic or gel-embedded diffusive processes.

To exploit the effect of reaction kinetics on the synthesis products, ionic strength and temperature are further parameters to investigate. Just like other reactions taking place between ions, the change of ionic strength most probably will affect the reaction rate. This effect, however, might be rather complex, since not only the rate of the liquid-phase reaction depends on ionic constituents but also the nucleation and crystal growth processes can be altered likewise. While the liquid-phase reactions between ions of unlike charge (i.e., all precipitation reactions) become slower with increasing ionic strength, crystal growth and aggregation usually are enhanced under those conditions. Furthermore, temperature-dependent kinetic measurements could be performed to determine the activation parameters of the reaction by applying the Eyring−Polányi equation.

ASSOCIATED CONTENT

Supporting Information

The Supporting Information is available free of charge at https://pubs.acs.org/doi/10.1021/acs.cgd.2c00265.

Experimental materials and protocols (kinetic experiments, XRD, SEM, IR, Raman, nitrogen adsorption); Sample characterization methods (XRD, SEM, IR, Raman, nitrogen adsorption); Calculated speciation diagrams; Fourier transformed infrared and Raman spectra and band assignments (PDF)

AUTHOR INFORMATION

Corresponding Author

Gábor Schuszter − *Department of Physical Chemistry and Materials Science, University of Szeged, Szeged H-6720, Hungary;* orcid.org/0000-0002-9170-9933; Email: schuszti@chem.u-szeged.hu

Authors

Edina Balog − *Department of Physical Chemistry and Materials Science, University of Szeged, Szeged H-6720, Hungary*

Gábor Varga − *Department of Physical Chemistry and Materials Science, University of Szeged, Szeged H-6720, Hungary;* orcid.org/0000-0002-7131-1629

Ákos Kukovecz − *Interdisciplinary Excellence Center, Department of Applied and Environmental Chemistry, University of Szeged, Szeged H-6720, Hungary;* orcid.org/0000-0003-0716-9557

Ágota Tóth − *Department of Physical Chemistry and Materials Science, University of Szeged, Szeged H-6720, Hungary;* orcid.org/0000-0001-8254-6354

Dezső Horváth − *Department of Applied and Environmental Chemistry, University of Szeged, Szeged H-6720, Hungary;* orcid.org/0000-0003-3852-6879

István Lagzi − *Department of Physics, Institute of Physics, Budapest University of Technology and Economics, Budapest H-1111, Hungary; MTA-BME Condensed Matter Research Group, Budapest H-1111, Hungary;* orcid.org/0000-0002-2303-5965

Complete contact information is available at: https://pubs.acs.org/10.1021/acs.cgd.2c00265

https://doi.org/10.1021/acs.cgd.2c00265
Cryst. Growth Des. 2022, 22, 4268−4276

Notes

The authors declare no competing financial interest.

■ ACKNOWLEDGMENTS

This work was supported by the National Research, Development and Innovation Office of Hungary (K138844 and K131425) and the National Research, Development, and Innovation Fund of Hungary under Grant TKP2021-EGA-02. E.B. thanks the ELTE Márton Áron Special College for financial support.

■ REFERENCES

(1) Furukawa, H.; Ko, N.; Go, Y. B.; Aratani, N.; Choi, S. B.; Choi, E.; Yazaydin, A.Ö.; Snurr, R. Q.; O'Keeffe, M.; Kim, J.; Yaghi, O. M. Ultrahigh Porosity in Metal-Organic Frameworks. *Science* **2010**, *329*, 424−428.

(2) Cheetham, A. K.; Férey, G.; Loiseau, T. Open-Framework Inorganic Materials. *Angew. Chem., Int. Ed.* **1999**, *38*, 3268−3292.

(3) Yaghi, O. M.; O'Keeffe, M.; Ockwig, N. W.; Chae, H. K.; Eddaoudi, M.; Kim, J. Reticular Synthesis and the Design of New Materials. *Nature* **2003**, *423*, 705−714.

(4) Furukawa, H.; Cordova, K. E.; O'Keeffe, M.; Yaghi, O. M. The Chemistry and Applications of Metal-Organic Frameworks. *Science* **2013**, *341*, 1230444.

(5) Smaldone, R. A.; Forgan, R. S.; Furukawa, H.; Gassensmith, J. J.; Slawin, A. M. Z.; Yaghi, O. M.; Stoddart, J. F. Metal−Organic Frameworks from Edible Natural Products. *Angew. Chem., Int. Ed.* **2010**, *49*, 8630−8634.

(6) Rosi, N. L.; Eckert, J.; Eddaoudi, M.; Vodak, D. T.; Kim, J.; O'Keeffe, M.; Yaghi, O. M. Hydrogen Storage in Microporous Metal-Organic Frameworks. *Science* **2003**, *300*, 1127−1129.

(7) Suh, M. P.; Park, H. J.; Prasad, T. K.; Lim, D.-W. Hydrogen Storage in Metal−Organic Frameworks. *Chem. Rev.* **2012**, *112*, 782−835.

(8) He, Y.; Zhou, W.; Qian, G.; Chen, B. Methane Storage in Metal−Organic Frameworks. *Chem. Soc. Rev.* **2014**, *43*, 5657−5678.

(9) Lin, Y.; Kong, C.; Zhang, Q.; Chen, L. Metal-Organic Frameworks for Carbon Dioxide Capture and Methane Storage. *Adv. Energy Mater.* **2017**, *7*, 1601296.

(10) Simmons, J. M.; Wu, H.; Zhou, W.; Yildirim, T. Carbon Capture in Metal−Organic Frameworks − a comparative study. *Energy Environ. Sci.* **2011**, *4*, 2177−2185.

(11) Lin, R.-B.; Xiang, S.; Xing, H.; Zhou, W.; Chen, B. Exploration of Porous Metal−Organic Frameworks for Gas Separation and Purification. *Coord. Chem. Rev.* **2019**, *378*, 87−103.

(12) Li, B.; Wang, H.; Chen, B. Microporous Metal−Organic Frameworks for Gas Separation. *Chem. - Asian J.* **2014**, *9*, 1474−1498.

(13) Gascon, J.; Corma, A.; Kapteijn, F.; Llabrés i Xamena, F. X. Metal−Organic Framework Catalysis: Quo vadis? *ACS Catal.* **2014**, *4*, 361−378.

(14) Yang, D.; Gates, B. C. Catalysis by Metal Organic Frameworks: Perspective and Suggestions for Future Research. *ACS Catal.* **2019**, *9*, 1779−1798.

(15) Hu, W.; Pattengale, B.; Huang, J. Zeolitic Imidazolate Frameworks as Intrinsic Lightharvesting and Charge Separation Materials for Photocatalysis. *J. Chem. Phys.* **2021**, *154*, 240901.

(16) Zheng, H.; Zhang, Y.; Liu, L.; Wan, W.; Guo, P.; Nyström, A. M.; Zou, X. One-pot Synthesis of Metal−Organic Frameworks with Encapsulated Target Molecules and Their Applications for Controlled Drug Delivery. *J. Am. Chem. Soc.* **2016**, *138*, 962−968.

(17) Della Rocca, J.; Liu, D.; Lin, W. Nanoscale Metal−Organic Frameworks for Biomedical Imaging and Drug Delivery. *Acc. Chem. Res.* **2011**, *44*, 957−968.

(18) Stassen, I.; Burtch, N.; Talin, A.; Falcaro, P.; Allendorf, M.; Ameloot, R. An Updated Roadmap for the Integration of Metal−Organic Frameworks with electronic devices and chemical sensors. *Chem. Soc. Rev.* **2017**, *46*, 3185−3241.

(19) Allendorf, M. D.; Schwartzberg, A.; Stavila, V.; Talin, A. A. A Roadmap to Implementing Metal−Organic Frameworks in Electronic Devices: Challenges and Critical Directions. *Chem. - Eur. J.* **2011**, *17*, 11372−11388.

(20) Campbell, M. G.; Dincă, M. Metal−Organic Frameworks as Active Materials in Electronic Sensor Devices. *Sensors* **2017**, *17*, 1108−1119.

(21) Kreno, L. E.; Leong, K.; Farha, O. K.; Allendorf, M.; Van Duyne, R. P.; Hupp, J. T. Metal−Organic Framework Materials as Chemical Sensors. *Chem. Rev.* **2012**, *112*, 1105−1125.

(22) Xu, W.; Yaghi, O. M. Metal−Organic Frameworks for Water Harvesting from Air, Anywhere, Anytime. *ACS Cent. Sci.* **2020**, *6*, 1348−1354.

(23) Yaghi, O. M.; Kalmutzki, M. J.; Diercks, C. S. *Introduction to Reticular Chemistry: Metal−Organic Frameworks and Covalent Organic Frameworks*; Wiley-VCH: 2019.

(24) Sun, Y.; Zhou, H.-C. Recent Progress in the Synthesis of Metal−Organic Frameworks. *Sci. Technol. Adv. Mater.* **2015**, *16*, 054202.

(25) Pachfule, P.; Das, R.; Poddar, P.; Banerjee, R. Solvothermal Synthesis, Structure, and Properties of Metal−Organic Framework Isomers Derived from a Partially Fluorinated Link. *Cryst. Growth Des.* **2011**, *11*, 1215−1222.

(26) Lee, Y.-R.; Kim, J.; Ahn, W.-S. Synthesis of Metal−Organic Frameworks: A Mini Review. *Korean J. Chem. Eng.* **2013**, *30*, 1667−1680.

(27) Saliba, D.; Ammar, M.; Rammal, M.; Al-Ghoul, M.; Hmadeh, M. Crystal Growth of ZIF-8, ZIF-67, and Their Mixed-Metal Derivatives. *J. Am. Chem. Soc.* **2018**, *140*, 1812−1823.

(28) Zakhia Douaihy, R.; Al-Ghoul, M.; Hmadeh, M. Liesegang Banding for Controlled Size and Growth of Zeolitic-Imidazolate Frameworks. *Small* **2019**, *15*, 1901605.

(29) Park, J. H.; Paczesny, J.; Kim, N.; Grzybowski, B. A. Shaping Microcrystals of Metal−Organic Frameworks by Reaction-Diffusion. *Angew. Chem.* **2020**, *59*, 10301−10305.

(30) Cravillon, J.; Schröder, C. A.; Nayuk, R.; Gummel, J.; Huber, K.; Wiebcke, M. Fast Nucleation and Growth of ZIF-8 Nanocrystals Monitored by Time-Resolved In Situ Small-Angle and Wide-Angle X-Ray Scattering. *Angew. Chem., Int. Ed.* **2011**, *50*, 8067−8071.

(31) Patterson, J. P.; Abellan, P.; Denny, M. S., Jr.; Park, C.; Browning, N. D.; Cohen, S. M.; Evans, J. E.; Gianneschi, N. C. Observing the Growth of Metal−Organic Frameworks by *in Situ* Liquid Cell Transmission Electron Microscopy. *J. Am. Chem. Soc.* **2015**, *137*, 7322−7328.

(32) Guo, W.; Xia, W.; Cai, K.; Wu, Y.; Qiu, B.; Liang, Z.; Qu, C.; Zou, R. Kinetic-Controlled Formation of Bimetallic Metal−Organic Framework Hybrid Structures. *Small* **2017**, *13*, 1702049.

(33) Kaur, H.; Mohanta, G. C.; Gupta, V.; Kukkar, D.; Tyagi, S. Synthesis and Characterization of ZIF-8 Nanoparticles for Controlled Release of 6-Mercaptopurine Drug. *J. Drug Delivery Sci. Technol.* **2017**, *41*, 106−112.

(34) Lee, Y.-R.; Jang, M.-S.; Cho, H.-Y.; Kwon, H.-J.; Kim, S.; Ahn, W.-S. ZIF-8: A Comparison of Synthesis Methods. *Chem. Eng. J.* **2015**, *271*, 276−280.

(35) Luzuriaga, M. A.; Benjamin, C. E.; Gaertner, M. W.; Lee, H.; Herbert, F. C.; Mallick, S.; Gassensmith, J. J. ZIF-8 Degrades in Cell Media, Serum, and some − but Not All − Common Laboratory Buffers. *Supramol. Chem.* **2019**, *31*, 485−490.

(36) Akimbekov, Z.; Katsenis, A. D.; Nagabhushana, G. P.; Ayoub, G.; Arhangelskis, M.; Morris, A. J.; Friščić, T.; Navrotsky, A. Experimental and Theoretical Evaluation of the Stability of True MOF Polymorphs Explains Their Mechanochemical Interconversions. *J. Am. Chem. Soc.* **2017**, *139*, 7952−7957.

(37) Rivera-Torrente, M.; Mandemaker, L. D. B.; Filez, M.; Delen, G.; Seoane, B.; Meirer, F.; Weckhuysen, B. M. Spectroscopy, Microscopy, Diffraction and Scattering of Archetypal MOFs: Formation, Metal Sites in Catalysis and Thin Films. *Chem. Soc. Rev.* **2020**, *49*, 6694.

https://doi.org/10.1021/acs.cgd.2c00265
Cryst. Growth Des. 2022, 22, 4268−4276

(38) Zhang, H.; Zhao, M.; Yang, Y.; Lin, Y. S. Hydrolysis and Condensation of ZIF-8 in Water. *Micropor. Mesopor. Mater.* **2019**, *288*, 109568.
(39) Jian, M.; Liu, B.; Liu, R.; Qu, J.; Wang, H.; Zhang, X. Water-based Synthesis of Zeolitic Imidazolate framework-8 with High Morphology Level at Room Temperature. *RSC Adv.* **2015**, *5*, 48433.
(40) Yao, J.; Chen, R.; Wang, K.; Wang, H. Direct Synthesis of Zeolitic Imidazolate Framework-8/chitosan Composites in Chitosan Hydrogels. *Micropor. Mesopor. Mater.* **2013**, *165*, 200−204.
(41) He, M.; Yao, J.; Liu, Q.; Wang, K.; Chen, F.; Wang, H. Facile Synthesis of Zeolitic Imidazolate Framework-8 from a Concentrated Aqueous Solution. *Micropor. Mesopor. Mater.* **2014**, *184*, 55−60.
(42) Perrin, D. D. *Dissociation Constants of Organic Bases in Aqueous Solution: Supplement 1972*; International Union of Pure and Applied Chemistry and Butterworths: 1972.
(43) Shi, Q.; Chen, Z.; Song, Z.; Li, J.; Dong, J. Synthesis of ZIF-8 and ZIF-67 by Steam-Assisted Conversion and an Investigation of their Tribological Behaviors. *Angew. Chem., Int. Ed.* **2011**, *50*, 672−675.
(44) Zheng, H.; Wu, D.; Wang, Y.; Liu, X.; Gao, P.; Liu, W.; Wen, J.; Rebrov, E. V. One-step Synthesis of ZIF-8/ZnO Composites Based on Coordination Defect Strategy and its Derivatives for Photocatalysis. *J. Alloys Compd.* **2020**, *838*, 155219.
(45) Hu, Y.; Kazemian, H.; Rohani, S.; Huang, Y.; Song, Y. In Situ High Pressure Study of ZIF-8 by FTIR Spectroscopy. *Chem. Commun.* **2011**, *47*, 12694−12696.
(46) Lin, L.; Zhang, T.; Liu, H.; Qiu, J.; Zhang, X. In Situ Fabrication of a Perfect Pd/ZnO@ZIF-8 Core−shell Microsphere as an Efficient Catalyst by a ZnO Support-induced ZIF-8 Growth Strategy. *Nanoscale* **2015**, *7*, 7615.
(47) Nordin, N. A. H. M.; Ismail, A. F.; Misdan, N.; Nazri, N. A. M. Modified ZIF-8 Mixed Matrix Membrane for CO_2/CH_4 Separation. *AIP Conf. Proc.* **2017**, *1891*, 020091.
(48) Kumari, G.; Jayaramulu, K.; Maji, T. K.; Narayana, C. Temperature Induced Structural Transformations and Gas Adsorption in the Zeolitic Imidazolate Framework ZIF-8: A Raman Study. *J. Phys. Chem. A* **2013**, *117*, 11006−11012.
(49) Das, N. P.; Müller, B.; Tóth, Á.; Horváth, D.; Schuszter, G. Macroscale Precipitation Kinetics: Towards Complex Precipitate Structure Design. *Phys. Chem. Chem. Phys.* **2018**, *20*, 19768.
(50) Guo, X.; Xing, T.; Lou, Y.; Chen, J. Controlling ZIF-67 Crystals Formation Through Various Cobalt Sources in Aqueous Solution. *J. Solid State Chem.* **2016**, *235*, 107−112.
(51) Xyla, A. G.; Giannimaras, E. K.; Koutsoukos, P. The Precipitation of Calcium Carbonate in Aqueous Solutions. *Colloids Surf.* **1991**, *53*, 241−255.
(52) Jiang, S.; ter Horst, J. H. Crystal Nucleation Rates from Probability Distributions of Induction Times. *Cryst. Growth Des.* **2011**, *11*, 256.
(53) Brandel, C.; ter Horst, J. H. Measuring Induction Times and Crystal Nucleation Rates. *Faraday Discuss.* **2015**, *179*, 199.
(54) Zahorán, R.; Kukovecz, Á.; Tóth, Á.; Horváth, D.; Schuszter, G. High-speed Tracking of Fast Chemical Precipitations. *Phys. Chem. Chem. Phys.* **2019**, *21*, 11345.
(55) Kolmykov, O.; Commenge, J. M.; Alem, H.; Girot, E.; Mozet, K.; Medjahdi, G.; Schneider, R. Microfluidic Reactors for the Size-controlled Synthesis of ZIF-8 crystals in Aqueous Phase. *Maters. Des.* **2017**, *122*, 31−41.
(56) Jin, C.-X.; Shang, H.-B. Synthetic Methods, Properties and Controlling Roles of Synthetic Parameters of Zeolite Imidazole Framework-8: A Review. *J. Solid State Chem.* **2021**, *297*, 122040.

Recommended by ACS

Lattice Modification and Morphological Control of Halide-Substituted *yqt*-Type Zeolitic Imidazolate Frameworks Zn_3mim_5X, with X = F, Br, Cl, or OH

Stephan Glante, Sebastian Bette, *et al.*
APRIL 20, 2022
CRYSTAL GROWTH & DESIGN
READ

Growth Pattern Control and Nanoarchitecture Engineering of Metal–Organic Framework Single Crystals by Confined Space Synthesis

Hao Li, Kui Shen, *et al.*
MAY 06, 2022
ACS CENTRAL SCIENCE
READ

Impact of Chemical Primers on the Growth, Structure, and Functional Properties of ZIF-8 Films

Juan A. Allegretto, Matias Rafti, *et al.*
APRIL 06, 2022
THE JOURNAL OF PHYSICAL CHEMISTRY C
READ

Polymorphism in Ionic Cocrystals Comprising Lithium Salts and l-Proline

Rana Sanii, Michael J. Zaworotko, *et al.*
MAY 03, 2022
CRYSTAL GROWTH & DESIGN
READ

Get More Suggestions >

https://doi.org/10.1021/acs.cgd.2c00265
Cryst. Growth Des. 2022, 22, 4268−4276